Bulletin of the Seismological Society of America, Vol. 96, No. 4B, pp. S38–S49, September 2006, doi: 10.1785/0120050825

Ⓔ

Three-Dimensional Compressional Wavespeed Model, Earthquake Relocations, and Focal Mechanisms for the Parkfield, California, Region

by Clifford Thurber, Haijiang Zhang, Felix Waldhauser, Jeanne Hardebeck, Andrew Michael, and Donna Eberhart-Phillips

Abstract We present a new three-dimensional (3D) compressional wavespeed (V_p) model for the Parkfield region, taking advantage of the recent seismicity associated with the 2003 San Simeon and 2004 Parkfield earthquake sequences to provide increased model resolution compared to the work of Eberhart-Phillips and Michael (1993) (EPM93). Taking the EPM93 3D model as our starting model, we invert the arrival-time data from about 2100 earthquakes and 250 shots recorded on both permanent network and temporary stations in a region 130 km northeast–southwest by 120 km northwest–southeast. We include catalog picks and cross-correlation and catalog differential times in the inversion, using the double-difference tomography method of Zhang and Thurber (2003). The principal V_p features reported by EPM93 and Michelini and McEvilly (1991) are recovered, but with locally improved resolution along the San Andreas Fault (SAF) and near the active-source profiles. We image the previously identified strong wavespeed contrast (faster on the southwest side) across most of the length of the SAF, and we also improve the image of a high V_p body on the northeast side of the fault reported by EPM93. This narrow body is at about 5- to 12-km depth and extends approximately from the locked section of the SAF to the town of Parkfield. The footwall of the thrust fault responsible for the 1983 Coalinga earthquake is imaged as a northeast-dipping high wavespeed body. In between, relatively low wavespeeds (<5 km/sec) extend to as much as 10-km depth. We use this model to derive absolute locations for about 16,000 earthquakes from 1966 to 2005 and high-precision double-difference locations for 9,000 earthquakes from 1984 to 2005, and also to determine focal mechanisms for 446 earthquakes. These earthquake locations and mechanisms show that the seismogenic fault is a simple planar structure. The aftershock sequence of the 2004 mainshock concentrates into the same structures defined by the pre-2004 seismicity, confirming earlier observations (Waldhauser *et al.*, 2004) that the seismicity pattern at Parkfield is long lived and persists through multiple cycles of mainshocks.

Online material: 3D V_p model and earthquake relocations.

Introduction

The long-anticipated occurrence of an **M** 6.0 earthquake at Parkfield, California, took place on 28 September 2004 (Bakun *et al.*, 2005; Langbein *et al.*, 2005). Due to the ongoing Parkfield Earthquake Prediction Experiment (Bakun and Lindh, 1985) the earthquake was recorded by a sizable array of seismic (and other) instrumentation that allows us to develop a new, higher resolution, three-dimensional (3D) tomographic model of the compressional wavespeed (V_p) of the crust surrounding Parkfield, from San Simeon on the 0southwest to Coalinga on the northeast (Fig. 1). We use this new 3D model to derive absolute locations for about 16,000 earthquakes from 1966 to 2005 and high-precision relative locations for 9,000 earthquakes from 1984 to 2005 and determine focal mechanisms for 446 earthquakes. In addition to refining our knowledge of the crustal structure and seismotectonics of this region, we anticipate that these results will facilitate the development of high-quality rupture models for the 2004 event.

Not only is this region well instrumented, but it has also been previously studied with 3D seismic wavespeed models

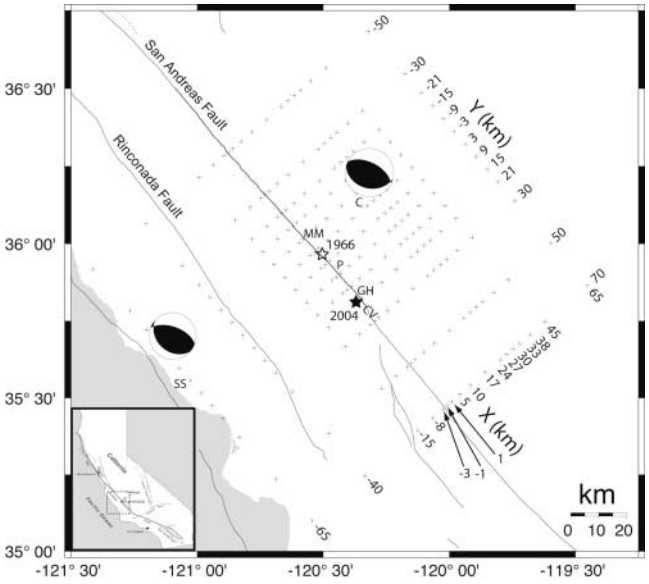

Figure 1. Map of the study area showing the locations of the towns of Parkfield (P), Coalinga (C), and San Simeon (SS), and other local features (MM, Middle Mountain; GH, Gold Hill; CV, Cholame Valley) and the inversion grid nodes (+) with *X* and *Y* coordinate values labeled. The open and filled stars are the 1966 and 2004 Parkfield mainshock epicenters, respectively, and focal mechanisms for the 1983 Coalinga and 2003 San Simeon earthquake are shown (source: Northern California Earthquake Data Center).

developed for the wider Parkfield region by Eberhart-Phillips and Michael (1993; henceforth EPM93) and for smaller regions centered on Middle Mountain by Michelini and McEvilly (1991; henceforth MM91) and Thurber *et al.* (2003, 2004). These studies, as well as Waldhauser *et al.* (2004), also presented detailed views of the seismicity of this region. EPM93 determined a wavespeed model for the largest area, so our model represents most closely an update of their work. This update is warranted because we are able to provide a higher-resolution model of the crustal structure and because we can examine the results in the context of the 2004 earthquake sequence, including comparisons to the 1966 Parkfield sequence. We can achieve a higher-resolution wavespeed model for three reasons. First, the aftershocks of the 2004 mainshock and the 2003 **M** 6.5 San Simeon earthquake (Hardebeck *et al.*, 2004) provide additional sources to illuminate the structure of this region. Second, increases in computational power allow us to simultaneously invert data from many more events. And third, new double-difference location (Waldhauser and Ellsworth, 2000) and tomography methods (Zhang and Thurber, 2003) allow us to include both catalog picks and cross-correlation and catalog differential times in the solutions for earthquake locations and 3D wavespeed structure.

Tomography Model

Dataset

The arrival-time and differential-time data utilized are from three sources. Travel times from the active-source profiles (Fig. 2a,b,) are from the compilation by Brocher (2003). These travel times are augmented with available catalog picks for the shots from the Northern California Earthquake Data Center (NCEDC) archive. The earthquake data (Fig. 2c) come from two main sources. One is a combination of NCEDC, PASO array (Thurber *et al.*, 2003, 2004), and Coalinga aftershock (Eberhart-Phillips, 1990) picks and corresponding "catalog" (i.e., not cross-correlation) differential times from the time period January 1980 to May 2005. The NCEDC and PASO earthquakes were selected on the basis of magnitude (>2.0) and spatial distribution. The other is a subset of the cross-correlation differential time dataset of Waldhauser *et al.* (2004) and corresponding catalog picks from the time period January 1984 to December 2002.

There are 2,374 events (255 shots and 2,119 earthquakes) and 923 stations used for our inversion, with a total of 80,823 absolute catalog times and 348,918 differential times. For the differential times, we chose event pairs whose interevent distances are smaller than 15 km but greater than 0.5 km, based on the catalog locations. The reason for the latter restriction is that if two events are too close, their ray paths nearly overlap everywhere, so that as a result, there is not much information from the differential time to resolve the structure. A related reason is to make the tomographic system more stable by not including the small differential partial derivatives from very close event pairs. The maximum number of neighbor events linked to one event is 10. We required there to be at least 8 observing stations in common (i.e., links) in order for two events to be linked together. There were 25 station links on average for each event pair, with a total number of linked event pairs of 15,271. The average distance between linked event pairs is 2.13 km. There are a total of 89,063 cross-correlation *P*-wave differential times from 755 earthquakes around the SAF.

Inversion Details

Taking the EPM93 3D model as our starting model, we adopt the same coordinate system origin (35°57.60′ N, 120°30.28′ W) but modify their *Y*-axis rotation from an azimuth of 137.2° to 139.2° to provide a better alignment with the SAF surface trace (Jennings, 1977) through the model region. We also expand the model to cover a region 130 km northeast-southwest by 120 km northwest-southeast (Fig. 1). Our inversion grid is also slightly modified from EPM93 to make the horizontal node spacing somewhat more uniform and to extend the model southwestward to San Simeon. In the *X* direction, nodes are positioned at −65, −40, −15, −8, −3, −1, 1, 5, 10, 17, 24, 27, 30, 33, 38, 45, and 65 km, and in the *Y* direction at −50, −30, −21, −15, −9, −3, 3, 9, 15, 21, 30, 50, and 70 km (Fig. 1). In the *Z* direction,

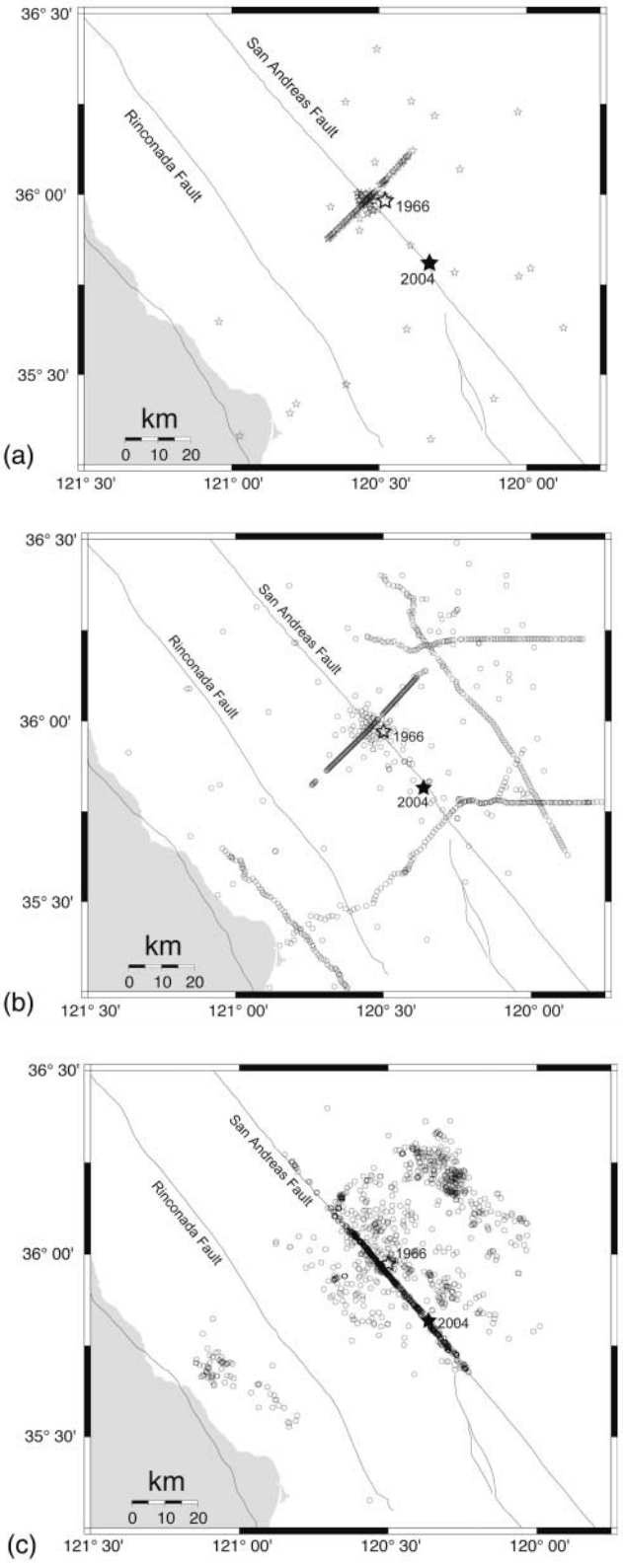

Figure 2. Maps of (a) shots (stars), (b) stations and active-source receivers (circles), and (c) earthquakes (circles) included in the inversion. The large open and filled stars are the 1966 and 2004 epicenters, respectively.

nodes are positioned at 0, 2, 4, 6, 9, 12, 16, 24, and 26 km relative to sea level (the deepest nodes allow for possible Moho refractions).

Preliminary inversions were carried out on the catalog data only using the algorithm simul2000 (Thurber and Eberhart-Phillips, 1999). This algorithm jointly solves for 3D wavespeed structure and earthquake locations using the first *P*-arrival times. This step was taken for data quality control purposes (mainly identifying poorly constrained events and picks with very high residuals) and to provide a formal but approximate estimate of wavespeed model resolution and uncertainty. The differential data were then added for inversions using the tomoDD algorithm (Zhang and Thurber, 2003). This algorithm jointly solves for 3D wavespeed structure and earthquake locations using both the first *P*-arrival times and the differential times, leading to improved resolution in the seismically active areas where the differential data provide dense sampling. The residual cutoff values, above which data are given zero weight, are 1.304 sec and 0.475 sec at the start of inversion for absolute and differential catalog times, respectively, and then are gradually reduced to 0.366 sec and 0.210 sec, respectively, at the end of inversion. There is no residual weighting for cross-correlation times at the start of inversion, and then after five iterations the residual weighting is applied with the residual cutoff value gradually decreasing from 0.237 sec to 0.042 sec. The smoothing constraint weightings in the horizontal and vertical directions are both 15. Initial and final root mean square (rms) arrival-time residuals (unweighted) are 165 msec and 62 msec for the absolute and differential catalog data and 202 msec and 9.8 msec for the cross-correlation data, corresponding to variance reductions of 86% for the catalog data and 99.8% for the cross-correlation data. Cross sections through the model are presented in Figures 3 and 4 and discussed in the Discussion section. (Ⓔ Higher resolution cross-sections, map-view slices, and a table of the 3D wavespeed model are available in the electronic edition of BSSA.)

Earthquake Relocation

We use the 3D wavespeed model to relocate ~3000 aftershocks of the 2004 Parkfield earthquake (through 17 August 2005), as well as 263 aftershocks of the 1966 **M** 6.0 Parkfield earthquake and ~13,000 background earthquakes in 1969–2004. To obtain the best absolute and relative relocations, the locations are done in two stages. First, *P*-wave arrival times are used to produce absolute locations for the events using the 3D wavespeed model and station corrections (Fig. 5). We generate the station corrections using a dataset of earthquakes and shots, including the events from the tomoDD inversion as well as additional events going back to the 1966 aftershock sequence. Then we use SIMULPS (Evans *et al.*, 1994) with the tomoDD velocity model fixed to relocate the earthquakes and solve for station corrections. Next, in an extension of Waldhauser *et al.* (2004),

approximately 9,000 events between 1 January 1984 and 30 June 2005 are relocated by applying the double-difference algorithm hypoDD (Waldhauser and Ellsworth, 2000) to a combination of cross-correlation differential times and travel-time differences formed from NCSN phase pick data (Fig. 6). (Ⓔ The complete list of stations used, the station corrections, and tables of the absolute locations and higher-resolution versions of Figures 5 and 6 are available in the electronic edition of BSSA.)

For the absolute locations, *P*-wave arrival times from the NCEDC database were used for the 2004 aftershocks and the background earthquakes. For the 1966 aftershocks, we used the *P*-wave arrival times picked by Eaton *et al.* (1970) from records from 19 U.S. Geological Survey (USGS) and Earthquake Mechanism Laboratory (U.S. Department of Commerce, Environmental Science Service Administration, San Francisco) portable stations and three University of California, Berkeley (UCB) permanent stations. Following the 2004 earthquake, the USGS deployed temporary stations at two of the 1966 portable sites (USGS stations 2 and 3 of Eaton *et al.* [1970]). Thus the 1966 and 2004 aftershocks sequences are recorded at three common sites, the two temporary stations and one permanent station (PGH at Gold Hill). The 1966 aftershocks and the earlier background seismicity are recorded at three common UCB stations (PRI, PRS, and LLA), as well as PGH. Because of these common stations, we were able to generate a common set of station corrections (derived using the 3D model), which allows us to more precisely locate the 1966 events relative to the 2004 aftershocks and the background seismicity.

For the relative locations, we use starting location and origin times from hypocenters determined in the 3D wavespeed model described above (Fig. 5), and use that model to evaluate partial derivatives and differential times in the double-difference inversion, using a version of hypoDD (Waldhauser, 2001) modified to incorporate a 3D model. Approximately 2 million *P*- and *S*-wave cross-correlation differential times, and 1.3 million catalog pick differential times, are used to relocate the events. The cross-correlation data are computed by applying the time domain method of Schaff *et al.* (2004) to all event pairs separated by less than 5 km. *S*-wave travel times are predicted by scaling the 3D *P*-wave model by a factor of 1.73. The resulting event locations are shown in Figure 6 in map view and cross sections.

Discussion of Relocation Results

The two sets of locations (Figs. 5, 6) are not dramatically different other than that the double-difference locations visually show a significantly greater degree of clustering. Both views are useful for characterizing the seismicity from 1966 to the present because evolving network characteristics, over almost 40 years, prevent us from producing such high-precision relative locations for the earlier events.

The seismicity is concentrated on a single planar fault surface at depth through Cholame Valley, where two principal fault traces are observed at the Earth's surface (Figs. 5 and 6) (Rymer *et al.*, 2006). The absolute locations place the earthquakes below the surface trace of the Southwest Fracture Zone (SWFZ) rather than the main surface trace of the SAF where surface creep is observed. This is consistent with the observation of coseismic slip in the 2004 mainshock on the SWFZ and only postseismic slip on the main trace (Rymer *et al.*, 2006). Unfortunately, the lack of shallow seismicity makes it unclear how the seismogenic fault at depth relates to the surficial fault traces. There is, however, a suggestion of a flower structure ("a series of vertical faults of compressional duplexes that are subparallel to the parent fault; the vertical faults divide upthrown blocks that spread near the surface in a manner resembling a flower" [Engelder, 1998]) in the vicinity of the 2004 mainshock (Fig. 6b, $Y = 20$ km). This hypothetical flower structure is a possible, and perhaps likely, connection from the single fault surface at depth to the Earth's surface, but this is not constrained by our results.

The spatial pattern of seismicity on the fault surface is quite complex and defines distinctive features that include subhorizontal streaks of seismicity, an abundance of repeating earthquakes, persistent clusters of earthquakes, and large regions devoid of microearthquakes (Waldhauser *et al.*, 2004) (Fig. 6a). The densest concentration of aftershocks occurs in the middle of the rupture along a 12-km-long streak (from kilometer 5 to kilometer 17 in Fig. 6a) between 4- and 6-km depth that can also be recognized in the preceding seismicity. The lack of reliably located events above this streak combined with coseismic slip below it and postseismic slip above it in 2004 (Murray and Langbein, 2006) suggests that it marks a transition in the stability field of the fault from velocity weakening to velocity strengthening behavior (Scholz, 2002).

Only a few small earthquakes occurred within a few hundred meters of the hypocenter prior to the mainshock, with the closest sizable cluster of microearthquakes about 4 km away to the southeast. The two M 5 aftershocks locate at the northwest end of the aftershock zone, within the "deep streak" of background seismicity beneath Middle Mountain (~kilometers -2 to $+6$ in Fig. 6a) at about 11-km depth as described by Waldhauser *et al.* (2004). The deep streak bounds the bottom of a prominent aseismic area that contains the 1934 and 1966 Parkfield earthquake hypocenters. This hole is partially bounded above by a second, smaller streak at about 7-km depth (~kilometer -2 to $+1$ in Fig. 6a). See Waldhauser *et al.* (2004) for further discussion.

While complex, the spatial pattern of seismicity is remarkably stationary over time despite stress changes due to two somewhat different mainshocks (Murray and Langbein, 2006). The aftershocks of both the 1966 and 2004 Parkfield earthquakes and the background seismicity are all similarly distributed. Note that the 1966 aftershocks did extend further north than those shown in Figure 5, but the more northerly

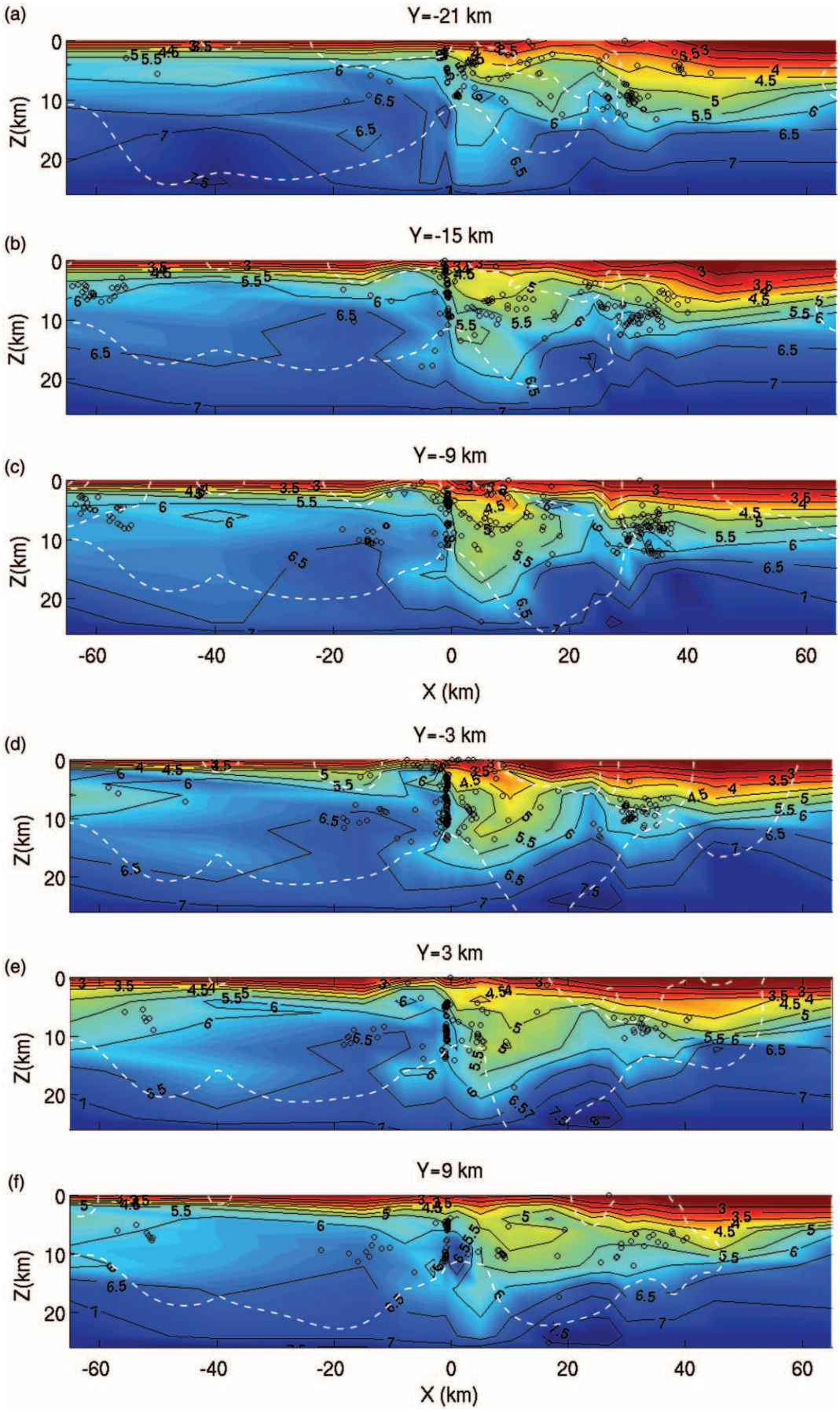
(a)
Y=-21 km
(b)
Y=-15 km
(c)
Y=-9 km
(d)
Y=-3 km
(e)
Y=3 km
(f)
Y=9 km
Z(km)
X (km)
0
10
20
-60
-40
-20
0
20
40
60

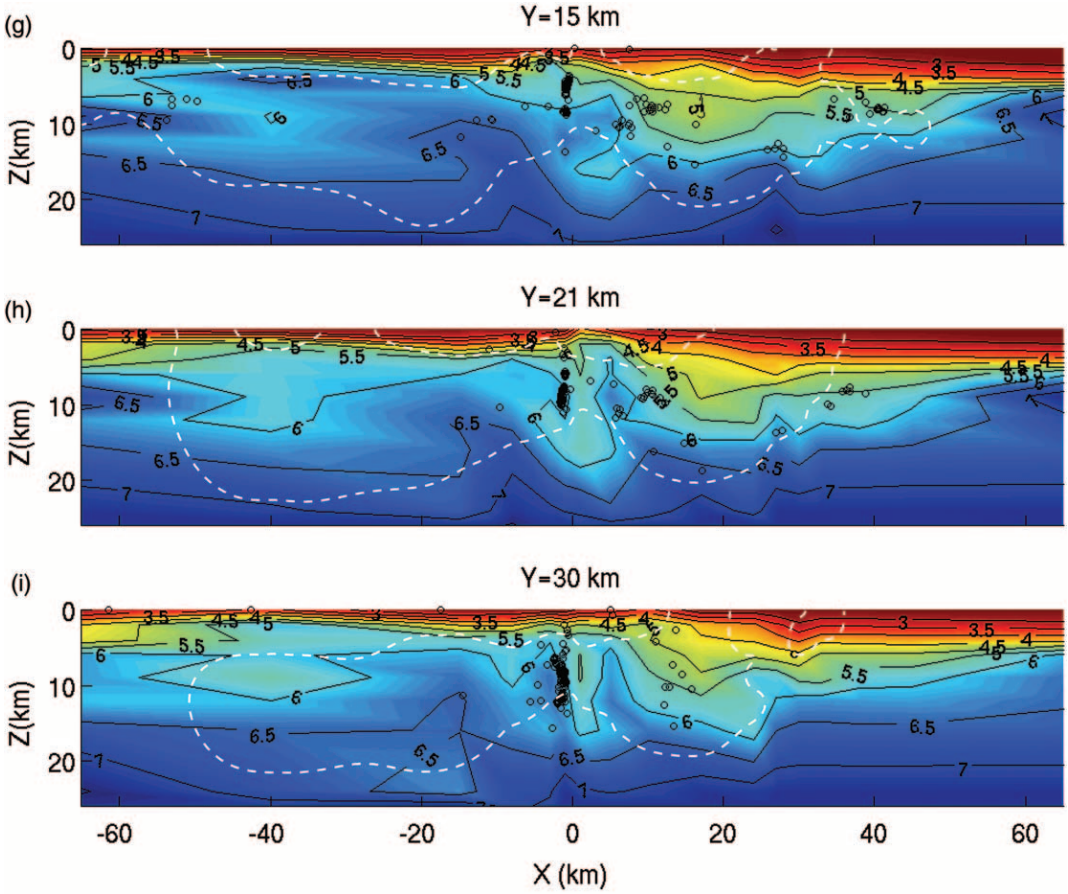

Figure 3. Fault-normal cross sections from $Y = -21$ km (northwest) to $Y = 30$ km (southeast). V_p is shown by black contours (labeled with km/sec) and colors from red (slow) to blue (fast). The white dashed contours show the limits of the region where the model is well resolved (resolution diagonal element > 0.4). Black circles are hypocenters of the earthquakes used in the V_p model inversion that are less than half the distance in the X direction to the adjacent section.

events are poorly located due to the relatively sparse station coverage there.

Earthquake Focal Mechanisms

We compute first-motion focal mechanism solutions using ray azimuths and takeoff angles found from ray tracing in the 3D seismic wavespeed model. The mechanisms were fit to *P*-wave polarity data (obtained from the NCEDC) using the technique of Hardebeck and Shearer (2002). This technique assigns mechanism quality based on the solution stability with respect to the expected uncertainty in the input parameters. We assume a polarity error rate of 10% (a combination of analyst errors and ray path errors; documented instrumental polarity reversals are corrected), which is consistent with the polarity misfit rate for well-constrained solutions, and we estimate the azimuth and takeoff angle uncertainty based on how much corresponding angles differ between the new 3D model and the model EPM93. We obtain good quality solutions (A and B of Hardebeck and Shearer [2002]) for 142 Parkfield aftershocks in September 2004–August 2005 and 304 background events in 1979–2004 (Fig. 7). About 75% of the solutions are consistent with pure strike-slip events on near-vertical planes aligned with the seismicity trend. Most of the remaining events have similar mechanism solutions except being somewhat oblique or on dipping planes, and a few events exhibit pure thrust or normal solutions. For events along the SAF zone, for only 4% of the mechanisms can we reject a null hypothesis of pure right-lateral slip on a vertical plane striking at 140° E of north at the 95% confidence level. Hence, both the background seismicity and the aftershocks are consistent with the overall SAF orientation and slip direction.

Discussion

The previously identified wavespeed contrast across the SAF is imaged along most of its length, with wavespeed contrasts (on the order of 1 km/sec) that are comparable to what has been reported (Fig. 3) (EPM93, MM91). The foot-

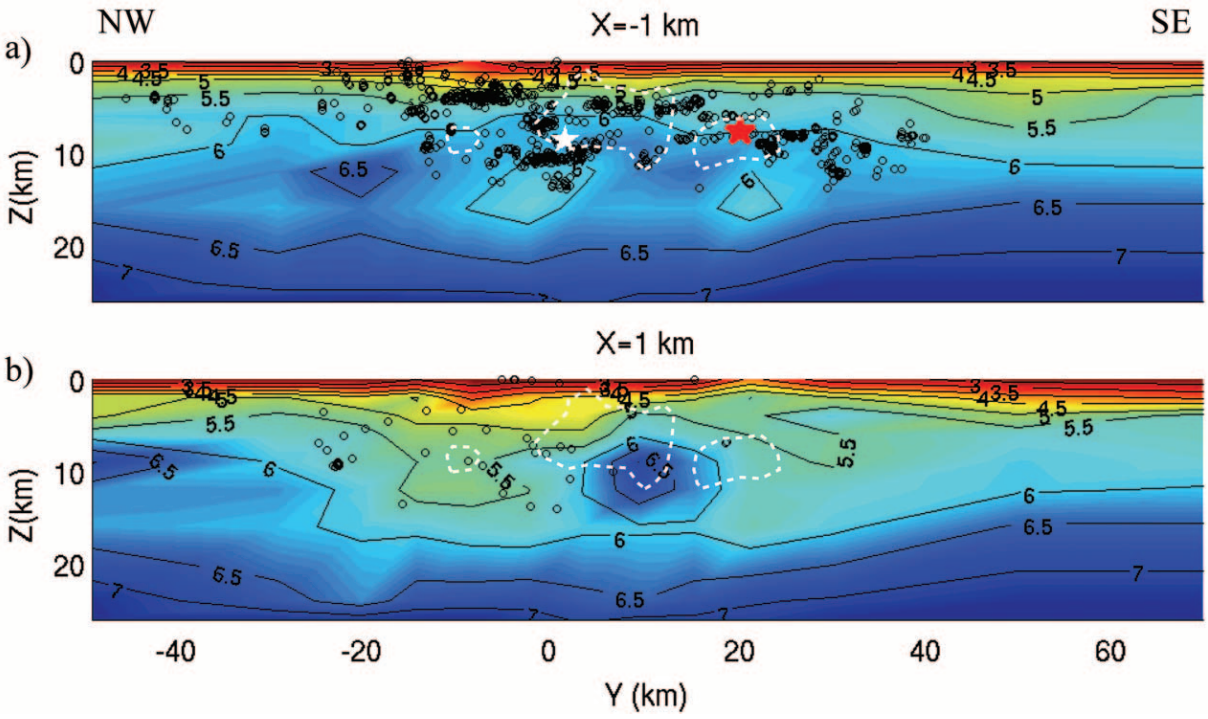

Figure 4. Fault-parallel cross sections at $X = -1$ km (southwest of the SAF trace) and $X = 1$ km (northeast of the SAF trace). V_p is shown by black contours (labeled with km/sec) and colors from red (slow) to blue (fast). The red and white stars are the hypocenters of the 2004 and 1966 Parkfield mainshocks, respectively, and black circles are hypocenters of the earthquakes used in the V_p model inversion. White dashed contours are the 10-cm contours from the mainshock slip model inverted from static GPS and 1-Hz GPS data and seismic waveforms (Langbein *et al.*, 2005).

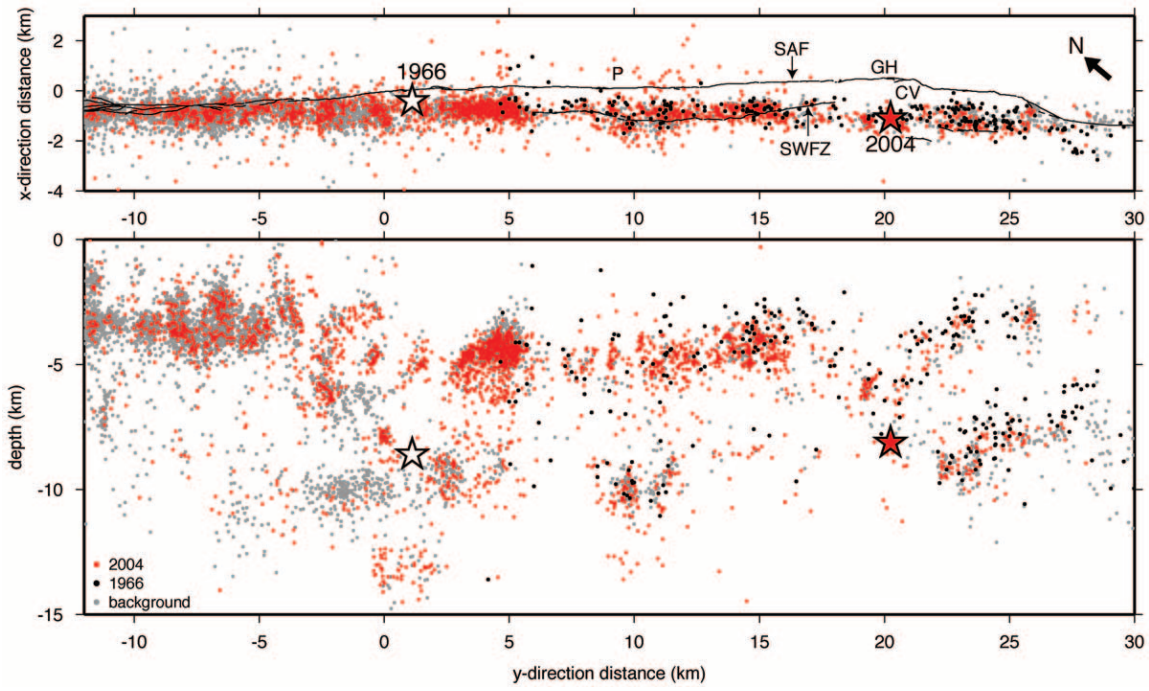

Figure 5. Single-event relocations of ~16,000 earthquake from 1966 to 2005 (rms residual < 0.1 sec), using the 3D V_p model and station corrections. P, town of Parkfield; GH, Gold Hill; CV, Cholame Valley; SAF, main trace of San Andreas; SWFZ, Southwest Fracture Zone. Red and white stars are the 2004 and 1966 hypocenters, respectively.

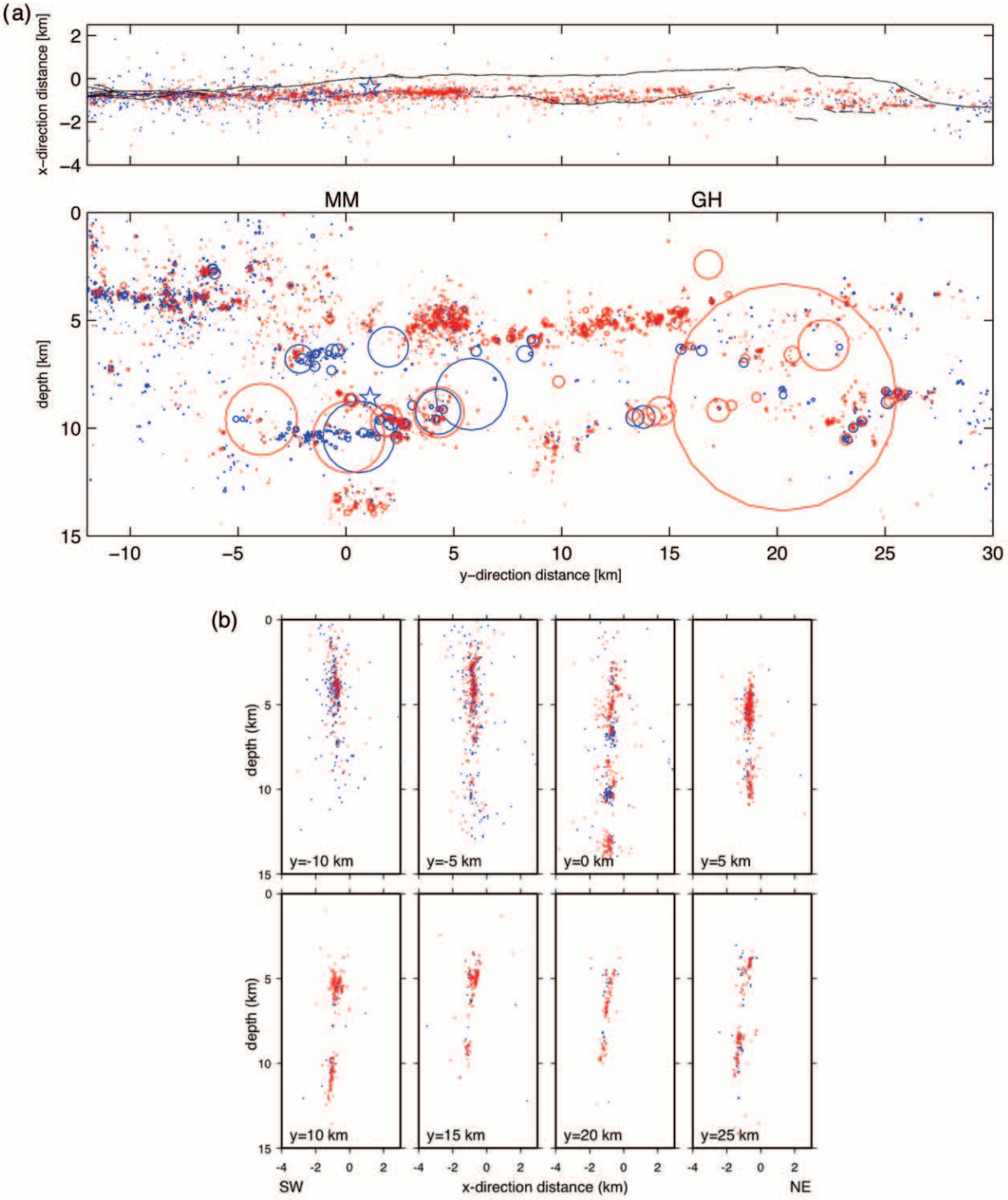

Figure 6. (a) Map and along-fault cross section and (b) fault-normal cross-sections of double-difference relocations of ~9,000 earthquakes from 1984 to 2005 using the 3D wavespeed model. Blue are events from 1984 to the 2004 mainshock, and red are the 2004 mainshock and its aftershocks. In the cross section in (a), symbols (circles) indicate size of a model circular source with a 30 bar stress drop. Star indicates location of 1966 hypocenter. MM, Middle Mountain; GH, Gold Hill.

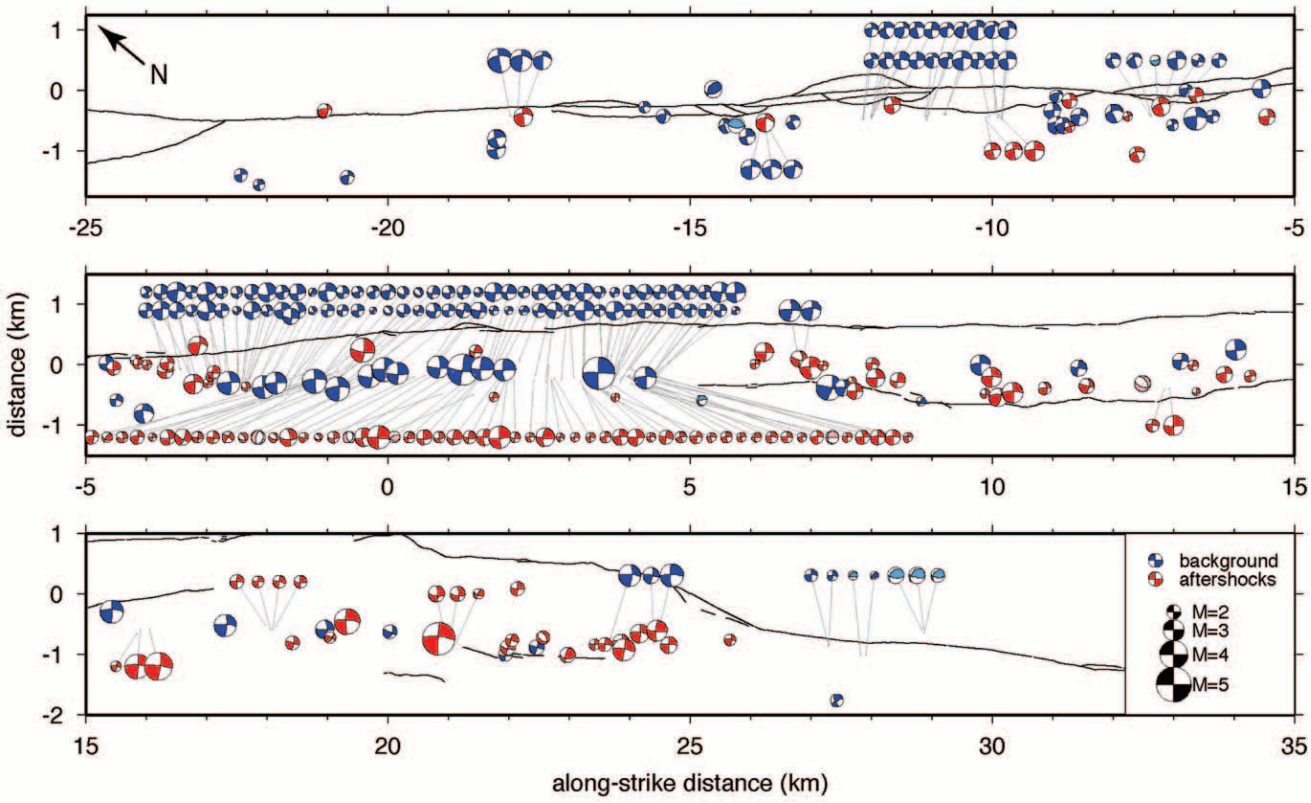

Figure 7. Strip maps of focal mechanisms for 442 events, 1979–2005. Background seismicity is in blue and the 2004 sequence is in red. Lightly shaded mechanisms (comprising 4% of the total) are those for which we can reject the null hypothesis of pure right-lateral slip on the SAF at the 95% confidence level.

wall of the thrust fault responsible for the 1983 Coalinga earthquake is imaged as a northeast-dipping high wavespeed body, similar to the results of Eberhart-Phillips (1990) (kilometers 20 to 40 in sections $Y = -21$ to $Y = 3$, Fig. 3a–e). Above the Coalinga fault plane and in between Coalinga and Parkfield, relatively low wavespeeds (<5 km/sec) extend to as deep as 10 km. The thick low wavespeed zone may be responsible in part for the greater ground shaking to the northeast of the SAF than to the southwest in the 2004 mainshock (Bakun *et al.*, 2005; Shakal *et al.*, 2005), given the relatively high V_p/V_s values associated with this zone (Michelini and McEvilly, 1991; Thurber *et al.*, 2003). Due to the broad similarity between our new model and the results of EPM93, we refer the reader to that article for detailed discussion of relationships among V_p, geology, and potential field data.

One value of this new model is that the higher-resolution images provide new insights into the seismogenic structure and behavior of this region. For instance, we more clearly image a high-V_p body on the northeast side of the SAF (Figs. 3f–i, 4b) identified previously by EPM93. EPM93 noted the apparent spatial relationship between this body and the primary slip patch in the 1966 mainshock, and between the high-V_p body and a 10–20 mgal isostatic residual gravity anomaly in the map of Snyder *et al.* (1982). We attribute our ability to image this feature more clearly than EPM93 (and MM91) to the abundant new earthquake data from the 2004 aftershock sequence (including differential times). Previous tomographic studies had to rely on relatively few events along the rupture zone.

The high maximum wavespeed (~6.6 km/sec) found at the northwestern part of the body is inconsistent with the high V_p Salinian rocks on the southwest side of the SAF that are expected to have a maximum wavespeed of ~6 km/sec. But this high wavespeed is consistent with the Permanente Terrane (Brocher, 2005), an oceanic sequence of mafic rocks overlain by limestone, chert, shale, and tuff. The Permanente Terrane was first identified in the Parkfield area, east of Gold Hill, by McLaughlin *et al.* (1996), and so we propose that the high-V_p body consists of the greenstones and mafic rocks of the Permanente Terrain.

The part of the high-V_p body that is closest to or apparently in contact with the SAF in our new image (Fig. 3f,g) appears to be spatially related to the area of primary slip (10 cm or more) in the 2004 mainshock (Fig. 4b) in the combined static GPS–1 Hz GPS–seismic solution of Lang-

bein *et al.* (2005), which is similar to (but smoother than) the strong-motion models of Custodio *et al.* (2005) and Liu *et al.* (this issue). Thus, this new model may clarify our view of how geologic structure imaged by seismic wavespeed models relates to seismogenic behavior (Michael and Eberhart-Phillips, 1991), as it indicates that high wavespeed bodies are present on both sides of the fault in association with the Parkfield rupture patch.

Further to the southeast, along the fault, the high-V_p body is visibly separated from the seismically active fault, with an evident low wavespeed zone along the SAF in between (Fig. 3h, i). This trend of this body away from the fault is consistent with gravity and magnetic anomalies (R. Jachens [personal comm., 2005]; based on potential field maps in Jachens *et al.* [1988] and McPhee *et al.* [2004]).

Despite the complex geologic structure surrounding the SAF (EPM93), the earthquake relocations and focal mechanisms reveal that the seismically active fault surface is predominantly a planar fault, and that fault surface underlies the SWFZ in Cholame Valley. Above depths shallower than the seismicity, however, the lack of earthquakes prevents us from being able to image how this planar fault surface connects to the multiple fault strands observed at the surface. Furthermore, there is no evidence that these multiple fault strands and the Cholame Valley step-over continue through to the seismically active part of the fault; thus any connection between them and the southern end of the Parkfield segment is more complex and currently enigmatic. This enigmatic relationship between fault segmentation and the surface traces introduces a note of doubt into attempts to use surface faulting as a basis for fault segmentation in seismic hazards assessment (Lindh and Boore, 1981; Bakun and McEvilly, 1984). Such doubts have previously been noted for the Calaveras Fault (Michael, 1988) and for the SAF at Parkfield (EPM93, Bakun *et al.*, 2005). We note that the new higher-resolution model and earthquake locations, including events through two mainshock sequences, leave these doubts intact.

Our locations reproduce the streaks, multiplets, and holes reported by Waldhauser *et al.* (2004) (Fig. 6). The similarities between the spatial patterns of the 1966 aftershocks and the background seismicity now extend to the 2004 aftershock sequence. While the occurrence of the **M** 6.0 Parkfield mainshocks increases the rate of seismicity, it does not appear to change their spatial pattern, and repeating earthquakes (microearthquakes with essentially identical waveforms, locations, and moments) (e.g., Nadeau *et al.*, 1995) continue to occur, although at temporarily increased rates. We infer from these observations that the seismogenic and nonseismogenic fault patches result from local differences in geometrical or rheological properties of the fault, as opposed to transient stress heterogeneity.

The limited amount of three-component data precludes the derivation of an adequate shear wavespeed (V_s) or V_p/V_s model for this large region. Most of the *S* data come from the High Resolution Seismic Network and the temporary PASO array, and thus are localized mainly within a few kilometers of the SAF. For purposes of synthetic seismogram generation, however, the V_p/V_s models of Thurber *et al.* (2003, 2004) and/or the V_p-V_s relationships of Brocher (2005) could be used to derive a rough estimate of the 3D V_s structure in the region.

Conclusions

The abundant aftershock activity following the 2004 Parkfield mainshock, increases in computation power, and the development of double-difference methods all contribute to an improved image of the 3D V_p structure and seismicity surrounding the rupture zone. The previously reported (e.g., EPM93, MM91) strong wavespeed contrast across the SAF (southwest side fast) is imaged in most places, with the primary exception being the general region of the 2004 Parkfield rupture zone, where a high-V_p body is present northeast of the fault. The cross-correlation differential times help sharpen the V_p image along the SAF and also resolve the seismicity streaks and multiplets reported previously in the double-difference location study of Waldhauser *et al.* (2004), as well as the predominantly simple planar fault imaged in that study and EPM93. A set of focal mechanisms that are dominated by pure strike-slip aligned with the SAF trend support the general simplicity of the SAF in this region, in contrast to the relatively complex surface trace (Rymer *et al.*, 2006). The Coalinga earthquake sequence is associated with a northeast-dipping high-V_p body, as observed previously (Eberhart-Phillips, 1990; EPM93). In between Coalinga and the SAF, there is a relatively deep zone of low V_p ($<$5 km/sec) extending to as much as 10-km depth. Spatial stationarity of seismicity features over the time period from the 1966 mainshock through much of the 2004 aftershock sequence indicates the existence of structural control(s) (geometrical and/or rheological) on the location of seismogenic patches, with time varying stress possibly controlling only the rate of seismicity.

Acknowledgments

This material is based on work supported by the National Science Foundation under Grant Nos. EAR-0346105 and EAR-0454511 (CT) and the USGS/NEHRP program under Grant No. 05HQGR0051 (FW). Catalog picks and focal mechanism parameters were obtained from the Northern California Earthquake Data Center (NCEDC); we thank Doug Neuhauser for his tireless efforts to maintain the NCEDC. We thank Tom Brocher, John Hole, and Trond Ryberg for providing active-source profile data; Bob Jachens, Darcy McPhee, and Tom Brocher for advice on geologic interpretation; David Schaff for his cross-correlation code; and guest editor Ruth Harris, Anthony Lomax, Robert Simpson, Paul Reasenberg, and an anonymous reviewer for their careful and constructive reviews. Figures 1 and 2 were generated with the Generic Mapping Tools (GMT) package (Wessel and Smith, 1991).

References

Bakun, W. H., and A. G. Lindh (1985). The Parkfield, California, earthquake prediction experiment, *Science* **229,** 619–624.

Bakun, W. H., and T. V. McEvilly (1984). Recurrence models and Parkfield, California earthquakes, *J. Geophys. Res.* **89,** 3051–3058.

Bakun, W. H., B. Aagaard, B. Dost, W. L. Ellsworth, J. L. Hardebeck, R. A. Harris, C. Ji, M. J. S. Johnston, J. Langbein, J. J. Lienkaemper, A. J. Michael, J. R. Murray, R. M. Nadeau, P. A. Reasenberg, M. S. Reichle, E. A. Roeloffs, A. Shakal, R. W. Simpson, and F. Waldhauser (2005). Implications for prediction and hazard assessment from the 2004 Parkfield, California, earthquake, *Nature* **437,** 969–974.

Brocher, T. M. (2003). Hypocentral accuracy of surficial detonations in northern California, *Seism. Res. Lett.* **74,** 12–19.

Brocher, T. M. (2005). Compressional and shear wave velocity versus depth in the San Francisco Bay Area, California: rules for USGS Bay Area velocity model 05.0.0, *U.S. Geol. Surv. Open-File Rept. 05-1317*, 58 pp.

Custodio, S., P. Liu, and R. J. Archuleta (2005). The 2004 Mw 6.0 Parkfield, California, earthquake: inversion of near-source ground motion using multiple data sets, *Geophys. Res. Lett.* **32,** L23312, doi 10.1029/2005GL024417.

Eaton, J. P., M. E. O'Neill, and J. N. Murdock (1970). Aftershocks of the 1966 Parkfield-Cholame, California, earthquake; a detailed study, *Bull. Seism. Soc. Am.* **60,** 1151–1197.

Eberhart-Phillips, D. (1990). Three-dimensional P and S velocity structure in the Coalinga region, California, *J. Geophys. Res.* **95,** 15,342–15,363.

Eberhart-Phillips, D., and A. J. Michael (1993). Three-dimensional velocity structure, seismicity, and fault structure in the Parkfield region, central California, *J. Geophys. Res.* **98,** 15,737–15,758.

Engelder, T. (1998). Structural geology class notes (GEOSC 465), http://www.geosc.psu.edu/~engelder/geosc465/notes465.html (last accessed May 2006).

Evans, J. R., D. Eberhart-Phillips, and C. H. Thurber (1994). User's manual for SIMULPS12 for imaging V_p and V_p/V_s: a derivative of the Thurber tomographic inversion SIMUL3 for local earthquakes and explosions, *U.S. Geol. Surv. Open File Rept. OFR 94-431*, 101 pp.

Hardebeck, J. L., and P. M. Shearer (2002). A new method for determining first-motion focal mechanisms, *Bull. Seism. Soc. Am.* **92,** 2264–2276.

Hardebeck, J. L., J. Boatwright, D. Dreger, R. Goel, V. Graizer, K. Hudnut, C. Ji, L. Jones, J. Langbein, J. Lin, E. Roeloffs, R. Simpson, K. Stark, R. Stein, and J. C. Tinsley (2004). Preliminary report on the 22 December 2003 M6.5 San Simeon, California, earthquake, *Seism. Res. Lett.* **75,** 155–172.

Jachens, R. C., C. M. Wentworth, and R. J. McLaughlin (1998). Pre-San Andreas location of the Gualala block inferred from magnetic and gravity anomalies, in *Geology and Tectonics of the Gualala Block, Northern California*, W. P. Elder (Editor) Society for Sedimentary Geology Tulsa, Oklahoma, 27–64.

Jennings, C. W. (1977). Geologic map of California, *Calif. Div. Mines Geol., Geologic Data Map 2*, scale 1:750,000.

Langbein, J., R. Borcherdt, D. Dreger, J. Fletcher, J. L. Hardebeck, M. Hellweg, C. Ji, M. Johnston, J. R. Murray, and R. Nadeau (2005). Preliminary report on the 28 September 2004, M 6.0 Parkfield, California earthquake, *Seism. Res. Lett.* **76,** 10–26.

Lindh, A. G., and D. M. Boore (1981). Control of rupture by fault geometry during the 1966 Parkfield earthquake, *Bull. Seism. Soc. Am.* **71,** 95–116.

Liu, P., S. Custodio, and R. J. Archuleta (2006). Kinematic inversion of the 2004 **M** 6.0 Parkfield earthquake including site effects, *Bull. Seism. Soc. Am.* **96,** no. 4B, S143–S158

McLaughlin, R. J., W. V. Sliter, D. H. Sorg, P. C. Russell, and A. M. Sarna-Wojcicki (1996). Large-scale right-slip displacement on the east San Francisco Bay region fault system, California: implications for location of late Miocene to Pliocene Pacific plate boundary, *Tectonics* **15,** 1–18.

McPhee, D. K., R. C. Jachens, and C. M. Wentworth (2004). Crustal structure across the San Andreas Fault at the SAFOD site from potential field and geologic studies, *Geophys. Res. Lett.* **31,** doi 10.1029/2003GL019363.

Michael, A. J. (1988). Effects of three-dimensional velocity structure on the seismicity of the 1984 Morgan Hill, CA aftershock sequence, *Bull. Seism. Soc. Am.* **78,** 1199–1221.

Michael, A. J., and D. Eberhart-Phillips (1991). Relations among fault behavior, subsurface geology, and three-dimensional velocity models, *Science* **253,** 651–654.

Michelini, A., and T. V. McEvilly (1991). Seismological studies at Parkfield, part I: Simultaneous inversion for velocity structure and hypocenters using cubic B-splines parameterization, *Bull. Seism. Soc. Am.* **81,** 524–552.

Murray, J., and J. Langbein (2006). Slip on the San Andreas fault at Parkfield, California, over two earthquake cycles and the implications for seismic hazard, *Bull. Seism. Soc. Am.* **96,** no. 4B, S283–S303.

Nadeau, R. M., W. Foxall, and T. V. McEvilly (1995). Clustering and periodic recurrence of microearthquakes on the San Andreas Fault at Parkfield, California, *Science* **267,** 503–507.

Rymer, M. J., J. C. Tinsley, J. A. Treiman, J. R. Arrowsmith, K. B. Clahan, A. M. Rosinski, W. A. Bryant, H. A. Snyder, G. S. Fuis, N. Toké, and G. W. Bawden (2006). Surface fault slip associated with the 2004 Parkfield, California, earthquake, *Bull. Seism. Soc. Am.* **96,** no. 4B, S11–S27.

Schaff, D. P., G. H. R. Bokelmann, W. L. Ellsworth, E. Zanzerkia, F. Waldhauser, and G. C. Beroza (2004). Optimizing correlation techniques for improved earthquake location, *Bull. Seism. Soc. Am.* **94,** 705–721.

Scholz, C. (2002). *The Mechanics of Earthquakes and Faulting*, Cambridge University Press, Cambridge, U.K., 471 pp.

Shakal, A., V. Graizer, M. Huang, R. Borcherdt, H. Haddadi, K.-W. Lin, C. Stephens, and P. Roffers (2005). Preliminary analysis of strong-motion recordings from the 28 September 2004 Parkfield, California earthquake, *Seism. Res. Lett.* **76,** 27–39.

Snyder, D. B., C. W. Roberts, R. W. Saltus, and R. F. Sikora (YEAR?). A magnetic tape containing the principal facts of 64,026 gravity stations in California, *U.S. National Technical Information Service Report PB82-168287*, 34 pp.

Thurber, C., and D. Eberhart-Phillips (1999). Local earthquake tomography with flexible gridding, *Comp. Geosci.* **25,** 809–818.

Thurber, C., S. Roecker, K. Roberts, M. Gold, L. Powell, and K. Rittger (2003). Earthquake locations and three-dimensional fault zone structure along the creeping section of the San Andreas Fault near Parkfield, CA: Preparing for SAFOD, *Geophys. Res. Lett.* **30,** doi 10.1029/2002GL016004.

Thurber, C., S. Roecker, H. Zhang, S. Baher, and W. Ellsworth (2004). Fine-scale structure of the San Andreas fault and location of the SAFOD target earthquakes, *Geophys. Res. Lett.* **31,** L12S02, doi 10.1029/2003GL019398.

Waldhauser, F. (2001). HypoDD: a computer program to compute double-difference earthquake locations, *U.S. Geol. Surv. Open-File Rept. 01-113*, 25 pp.

Waldhauser, F., and W. L. Ellsworth (2000). A double-difference earthquake location algorithm: method and application to the Northern Hayward Fault, California, *Bull. Seism. Soc. Am.* **90,** 1353–1368.

Waldhauser, F., W. Ellsworth, D. P. Schaff, and A. Cole (2004). Streaks, multiplets, and holes: high-resolution spatio-temporal behavior of Parkfield seismicity, *Geophys. Res. Lett.* **31,** L18608, doi 10.1029/2004GL020649.

Wessel, P., and W. H. F. Smith (1991). Free software helps map and display data, *EOS Trans. AGU* **72,** 441.

Zhang, H., and C. H. Thurber (2003). Double-difference tomography: the method and its application to the Hayward fault, California, *Bull. Seism. Soc. Am.* **93,** 1875–1889.

Department of Geology and Geophysics
University of Wisconsin–Madison
1215 W. Dayton Street
Madison, Wisconsin 53706
(C.T, H.Z.)

Lamont Doherty Earth Observatory
P.O. Box 1000
61 Route 9W
Palisades, New York 10964-1000
(F.W.)

U.S. Geological Survey
345 Middlefield Road
Menlo Park, California 94025
(J.H., A.M.)

Institute for Geological and Nuclear Sciences Limited
Dunedin Research Centre
764 Cumberland Street
Private Bag 1930
Dunedin, New Zealand
(D.E.-P.)

Manuscript received 23 September 2005.